Coherent x-ray diffraction imaging of grown-in antiphase boundaries in $Fe_{65}Al_{35}$

Lorenz-M. Stadler,[1,*] Ross Harder,[2] Ian K. Robinson,[2] Christian Rentenberger,[1] H.-Peter Karnthaler,[1] Bogdan Sepiol,[1] and Gero Vogl[1]

[1]*Fakultät für Physik, Universität Wien, Strudlhofgasse 4, 1090 Wien, Austria*

[2]*London Centre for Nanotechnology and Department of Physics and Astronomy, University College, London, WC1E 6BT, United Kingdom*

(Received 22 February 2007; revised manuscript received 8 May 2007; published 30 July 2007)

Coherent x-ray diffraction has been used to image grown-in antiphase boundaries (APB's) in a metal alloy, which represent pure phase objects. The fine structure within the (001) superstructure diffraction peak of a *B*2-ordered bulk $Fe_{65}Al_{35}$ sample was inverted by means of iterative algorithms that Fourier transform between reciprocal and real space, applying appropriate constraints in each domain. Since the sample object is noncompact, bigger than the beam footprint, knowing the precise beam profile was essential to define the real-space constraint. Even though a unique long-range structure could not be derived, the algorithm found phase structures that were locally unique. These were identified in all reconstruction runs by means of a cross-correlation analysis. The obtained characteristic APB morphology is confirmed by transmission electron microscopy results from the same sample, revealing nearly planar APB walls on {110} planes terminating at grown-in dislocations.

DOI: 10.1103/PhysRevB.76.014204 PACS number(s): 61.10.Nz, 42.30.Rx, 61.66.Dk

I. INTRODUCTION

Depending on the temperature and on their exact composition, intermetallic alloys often exhibit superstructures that are based upon Bravais lattices. Usually, this higher order is not perfectly established over the whole crystal, since the superstructure starts to grow from different nucleation sites in the sample. Consequently, antiphase domains (APD's) form that are separated by antiphase-domain boundaries (APB's). Due to this disorder, scattering of coherent x rays produces an intensity modulation—a so-called speckle pattern—in the superstructure peaks, which is in direct relation to the exact arrangement of the scattering centers.

On the one hand, this intimate relation between the recorded diffraction pattern and the real-space structure makes possible the study of dynamical processes, since the speckle intensity is modified if the scattering-center arrangement changes. Analyzing the temporal correlations in the speckle-intensity fluctuations yields information about the underlying dynamics. In recent works this so-called x-ray intensity fluctuation spectroscopy (XIFS), which is also known as x-ray photon correlation spectroscopy (XPCS), was used in order to follow ordering kinetics and APD coarsening, respectively, in the $L1_2$-ordered alloy Cu_3Au (Ref. 1) and in a long-period superlattice Cu-Pd alloy.[2] Furthermore, quasiequilibrium APD fluctuations were studied in the *B*2-ordered $Co_{60}Ga_{40}$ intermetallic phase.[3]

On the other hand, one could ask whether it is possible to retrieve the information about the actual exact position of the scattering centers—and thus to overcome the famous phase problem—even though the APD and APB structure, respectively, is in general nonperiodic. Apart from the fundamental point of view, using coherent x rays for imaging APB structures would also be an interesting alternative to transmission-electron microscopy (TEM). The necessary thinning procedures in the TEM sample preparation impose a certain probability that delicate structures like APB's are disturbed. Moreover, the domains can be quite large—much larger than the sample thickness acceptable for TEM investigations. X rays, on the other hand, can probe much thicker specimens.

The problem of reconstructing the structure of an isolated ("compact") nonperiodic object from its coherent x-ray diffraction pattern alone has attracted increasing attention in recent years. The field is known as coherent x-ray diffraction imaging and as diffraction microscopy. Instead of lenses, algorithms are used that transform back and forth between real and reciprocal space, applying appropriate constraints in each domain.[4,5] Thereby, the resolution is—at least in principle—diffraction limited only. The condition that must be met is to "oversample" the diffraction pattern. This is expressed in the requirement that the oversampling ratio $\sigma = N/S$ must be greater equal 2, where N is the number of pixels in the detector and S is the number of pixels the real-space object occupies, the so-called support of the object.

Miao and co-workers showed the feasibility of recovering a two-dimensional noncrystalline sample using coherent soft x rays in small-angle x-ray scattering (SAXS) geometry.[6] Recently, Chapman and colleagues managed to accomplish such a measurement in a single-shot experiment, using a femtosecond pulse of soft x rays from the FLASH free-electron laser facility at DESY in Hamburg, Germany.[7] One experimental difficulty when doing such experiments in SAXS geometry is to record photons scattered at very small angles, since one must block the direct beam in order not to destroy the detector, usually. Thus, essential information on the overall dimensions of the sample may be lost, and there are endeavors to overcome this problem by means of clever algorithms.[8,9] A different approach, working for crystalline samples, was presented by Robinson *et al.*, where the oversampled speckle pattern around a Bragg peak of a gold nanocrystal was used to reconstruct the two-dimensional (2D) projection of the nanocrystal's shape.[10] Furthermore, x rays provide the opportunity to investigate thick samples due to their high penetration, actually making possible three-dimensional (3D) imaging. The latter was demonstrated for

artificial nanostructures measured in SAXS geometry[11,12] and for Au nanocrystals, where diffraction patterns were recorded around a Bragg peak.[13,14]

Coming back to the problem of imaging APB's one faces two major difficulties. First, antiphase domains are usually established over a whole crystal—either bulk or a thin film—and are not constrained to a small compact volume. In that sense one must deal with a noncompact object and only the beam profile defines the specific sample volume that is probed. Thus, an exact knowledge of the beam profile is mandatory. Second, APB's are pure phase objects, since adjacent antiphase domains essentially have the same electron density because the same kinds of atoms are present in each domain. The contrast between the domains results from the different phase shift the scattered photons get from two adjacent domains. Thus the APB structure is mirrored in the reconstructed phases only. However, in most of the works found in the literature only the electron density of the object is considered. The fact that the electron density is a real quantity provides an additional real-space constraint and improves the convergence of the reconstruction algorithms. Only in some cases have people thought about reconstructing a complex quantity, e.g., in order to get information on strain fields in nanocrystalline samples.[15,16] We note that the problem of noncompactness can possibly be overcome using the so-called Ptychography technique, which is the simultaneous inversion of diffraction patterns measured from overlapping regions of the sample.[17] The feasibility of using that method with hard x rays was demonstrated by Rodenburg and coworkers just recently.[18]

Up to now there is only a theoretical study which reports the successful reconstruction of antiphase domain structures in the classical Cu_3Au system.[19] Attempts to reconstruct antiphase domains from experimental data did not yield satisfying results.[20]

Finally, it should be mentioned that there is a paper that reports a successful solution to the similar problem of reconstructing strain profiles across a thin ordered $Cu_3Au(111)$ film, epitaxially grown on Al_2O_3.[21] In this case the density function of a $Cu_3Au(111)$ layer, stacked between a Nb(110) buffer and a Nb(110) cap, was modeled in the form of two Fermi step functions. The real space constraint was thus not only a support, but the whole calculated image, and the original Gerchberg-Saxton algorithm[4] could be used to retrieve the phase and determine the strain profiles.

In this paper, we report on coherent x-ray diffraction imaging of grown-in APB's in $B2$-ordered $Fe_{65}Al_{35}$. Thereby, knowing the illumination function, which comprises the real-space image, is key. In the present case, the illumination function was *measured* using an optical microscope. Although a consistent long-range structure is not retrieved, local unique APB's are unambiguously identified by means of a cross-correlation technique. The results are supported by TEM measurements.

The paper is organized as follows. In Sec. II, experimental details are given. An explanation of the observed speckle pattern is presented in Sec. III. Section IV describes the phasing procedure and further data treatment. The results are compared to TEM measurements and discussed in Sec. V. Section VI concludes the paper.

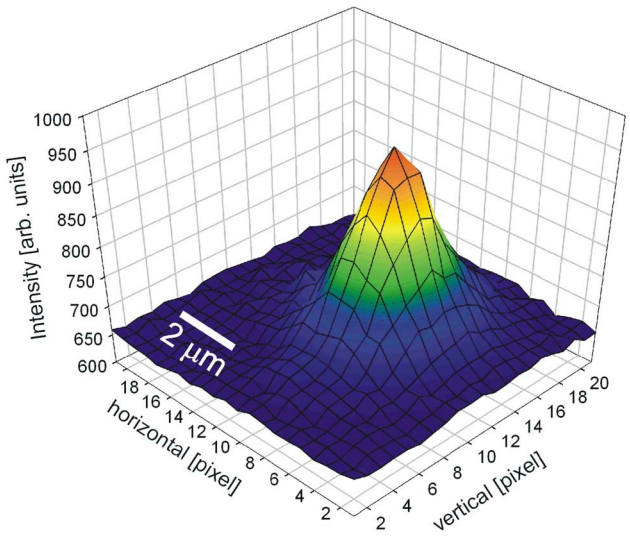

FIG. 1. (Color online) Measured illumination function $f(x,y)$. The size of one pixel was 0.45×0.45 μm^2.

II. EXPERIMENTAL DETAILS

Although a little bit off stoichiometry, $Fe_{65}Al_{35}$ still exhibits the $B2$ structure.[22] The $B2$ (or CsCl) structure is a body-centered-cubic crystal structure, where one sort of atoms sits in the cube center, whereas atoms of the other sort occupy the cube corners. Two types of APD's occur where the domains differ by a $\langle \frac{1}{2}\frac{1}{2}\frac{1}{2} \rangle$ shift in {110} planes. Thus, photons scattered at adjacent antiphase domains get phase shifts that differ by π.

The sample was grown using the Bridgman technique and consisted of a semicircular platelet, about 1 mm thick, with the normal of the polished surface parallel to $\langle 001 \rangle$. Several annealing steps at up to 725 °C resulted in a well-ordered crystal and μm-large APD's were expected.

The coherent x-ray diffraction measurements were done at the undulator beamline 34-ID-C at the Advanced Photon Source in Argonne, Illinois. Roller-blade slits[23] were used to predefine the beam to 20 μm in horizontal and 50 μm in vertical direction. A fluorescent plate was put at the sample position in order to image the beam. An optical microscope connected to a CCD camera (0.45 μm resolution) was used to control the further beam focusing with Kirkpatrick-Baez mirrors.[24] For taking the final coherent x-ray diffraction patterns, the roller-blade slits were closed down to 2.5×2.5 μm^2, which did not affect the illumination function, but improved the coherence properties of the beam. The final beam shape is shown in Fig. 1. This illumination function $f(x,y)$ could be fitted with a two-dimensional Gaussian

$$f(x,y) \propto \frac{1}{2\pi\sigma_x\sigma_y} \exp\left(-\frac{(x-x_0)^2}{2\sigma_x^2}\right)\exp\left(-\frac{(y-y_0)^2}{2\sigma_y^2}\right) \quad (1)$$

with full widths at half-maximum slightly different for the horizontal ($w_h=2.84\pm0.03$ μm) and the vertical direction ($w_v=3.26\pm0.03$ μm).

The sample was aligned with both the surface normal $\langle 001 \rangle$ and $\langle 110 \rangle$ in the scattering plane, and $\langle 001 \rangle$ was paral-

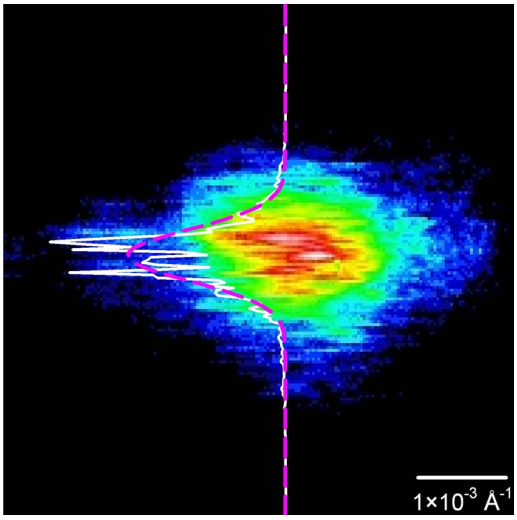

FIG. 2. (Color online) Central part (200×200 pixels) of the high-resolution image of the $Fe_{65}Al_{35}$ (001) superstructure reflection on a logarithmic pseudocolor intensity scale. The direction of the scattering angle 2Θ is vertical. The full white line is a slice along the 2Θ direction, exhibiting strong intensity modulations. The dashed (pink) line is a Gaussian fit to the slice with a FWHM of 23.9±0.6 pixel ($\Delta Q/\text{pixel} \approx 2.9\times10^{-5}$ Å^{-1}).

lel to the scattering vector. A direct illumination CCD camera (Princeton Instruments, 1340×1300 pixels, pixel size 22.5×22.5 μm^2), mounted at a distance of 3.29 m from the sample on the goniometer arm, was used to measure the (001) superstructure reflection, where the geometry was symmetric and scattering was in the vertical plane.

In order to realize the exact Bragg condition, i.e., to find the center of the superstructure reflection, the x-ray energy was varied over a certain range by closing and opening the undulator gap. For each new energy a frame was recorded and finally the one with the highest intensity was considered to be closest to the exact position of the reciprocal lattice point (001). Figure 2 shows the (001) peak in the central part (200×200 pixels) of the 400×400 pixel array ($\Delta Q/\text{pixel} \approx 2.9\times10^{-5}$ Å^{-1}), which was later used for the reconstruction procedure. Additionally, a slice through the peak along the 2Θ direction is shown, together with a Gaussian fit with a full width at half maximum (FWHM) of 23.9±0.6 pixel. The x-ray energy was 8.406 keV (λ=1.475 Å) with an energy resolution of $\Delta E/E \approx 10^{-4}$. Given a lattice constant of a=2.895 Å (Ref. 25) and hence a mass density of about 6.26 g/cm^3 the absorption length was $\mu \approx 7.2$ μm.[26] Thus, the information depth t was

$$t = \tfrac{1}{2}\mu \sin\Theta \approx 0.92\ \mu\text{m}, \tag{2}$$

with Θ=14.76°. This information depth compares with the Scherrer width of the peak and, thus, basically one ply of antiphase domains should have given rise to the measured speckle pattern in Fig. 2.

III. EXPLANATION OF THE OBSERVED SPECKLE PATTERN

Before coming to the reconstruction part it is desirable to understand why this particular speckle structure, elongated

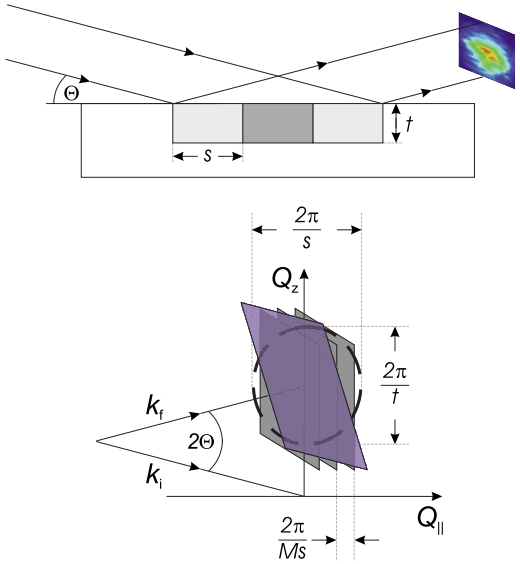

FIG. 3. (Color online) Top: schematic of the scattering at different domains (light and dark gray). Bottom: picture in reciprocal space with $\boldsymbol{k}_i$ the incoming and $\boldsymbol{k}_f$ the outgoing wave vector. The domains give rise to sheets of diffraction intensity (dark gray). The dashed ellipse indicates the extension of the speckled peak. The width along $\boldsymbol{Q}_z$ is related to the information depth by $2\pi/t$. The width along $\boldsymbol{Q}_\parallel$ is determined by the domain size according to $2\pi/s$. The typical distance between the sheets, i.e., the mean speckle size along $\boldsymbol{Q}_\parallel$, is given by $2\pi/(Ms)=2\pi/w_\parallel$. The CCD detector (transparent blue with its surface normal antiparallel to $\boldsymbol{k}_f$) cuts through these sheets under an angle of Θ.

normally to the 2Θ direction, is observed. The following analysis is based on Ref. 27. Looking at the diffraction pattern we can identify $M=3$, maybe 4 distinct speckles and the number of contributing APD's and APB's, respectively, must be of the same order. The shape of the x-ray beam spot on the sample is elongated along the beam direction by a factor of $1/\sin\Theta$. Therefore, the width of the spot along the beam direction, $w_\parallel$, is

$$w_\parallel = w_v/\sin\Theta \approx 12.8\ \mu\text{m}. \tag{3}$$

Hence a domain size and a mean distance between APB's, respectively, of about $s_{M=3} \approx 4.3$ μm is expected. This value is greater than the beam size perpendicular to the beam direction, $w_\perp$, which is simply $w_\perp = w_h$. Also the information depth t is much smaller. Such a real-space structure gives rise to diffraction spots strongly elongated along $\boldsymbol{Q}_z$, which is perpendicular to the sample surface, and one gets sheets of diffraction intensity in reciprocal space, illustrated in Fig. 3. Our two-dimensional CCD detector cuts at an angle of Θ through these sheets, producing the striped speckle structure that is observed in the measurement.

Consequently, the exact width of the peak along $\boldsymbol{Q}_z$ is not directly accessible. The typical speckle width along $\boldsymbol{Q}_\parallel$ is estimated by $2\pi/w_\parallel \approx 4.9\times10^{-5}$ Å^{-1}. On the detector we see the projection and thus must divide the above value by sin Θ. Therefore, we expect a speckle width along the 2Θ direction of about 6.6 pixel on the CCD camera. Looking closely at

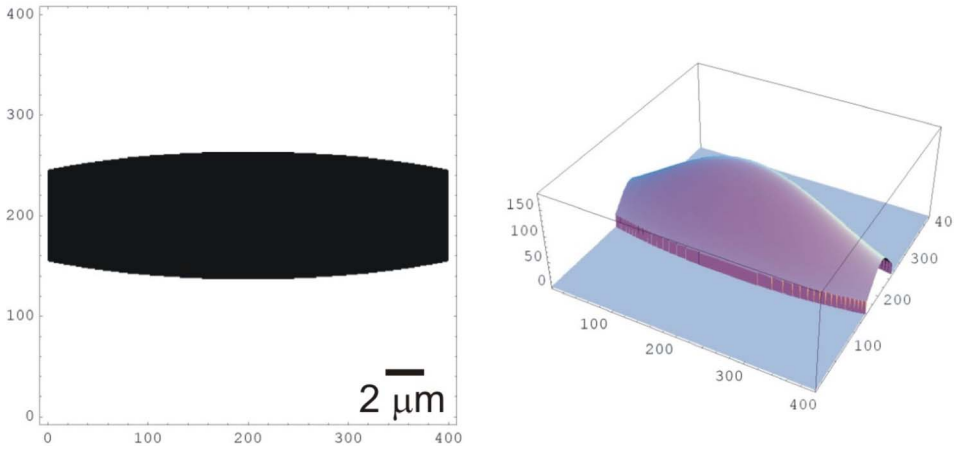

FIG. 4. (Color online) Illustration of the applied real-space constraints in the reconstruction procedure. Left-hand side: support (black) for the HIO cycles, defined by Eq. (4). Right-hand side: real-space amplitude used for the GS cycles, defined by Eq. (5).

the recorded diffraction pattern one has the impression that the measured speckle width is about 1 pixel smaller, i.e., the estimate is not perfect, but roughly correct. The overall peak width along $\boldsymbol{Q}_{\parallel}$ is given by $2\pi/s \approx 14.6 \times 10^{-5}$ Å^{-1}. Taking the projection into account we can expect 19.8 pixel peak width along the 2Θ direction on the CCD detector. This value is a little bit smaller than the 23.9 pixel FWHM of the Gaussian fit in Fig. 2. However, if we had taken $M=4$ instead of $M=3$ for our estimations, the expected peak width would have been 26.6 pixel. The rest of our interpretation would have remained unchanged.

IV. PHASING PROCEDURE AND FURTHER DATA TREATMENT

As it was mentioned in the introduction the phasing algorithms transform between reciprocal and direct space, thereby applying appropriate constraints in each domain. In reciprocal space the constraint consists always of the measured diffraction amplitudes $|F(\boldsymbol{Q})|$, with $\boldsymbol{Q}$ the scattering vector. In the very first step one starts by adding random phases to $|F(\boldsymbol{Q})|$, which gives $G_1(\boldsymbol{Q})$. Then the following four steps are looped: (i) substitution of the reciprocal-space amplitudes by the measured ones, giving $G_1'(\boldsymbol{Q})$, (ii) Fourier transform into real space, yielding the real-space estimate $g_1'(\boldsymbol{x})$, (iii) application of real-space constraints, giving $g_2(\boldsymbol{x})$, and (iv) Fourier transform back into reciprocal space, yielding the reciprocal-space estimate $G_2(\boldsymbol{Q})$.

In order to improve convergence one usually applies alternating periods of a certain number of iterations of a particular algorithm with particular real-space constraints. The most popular choice is to alternate between cycles of error reduction,[5] which is a derivative of the original Gerchberg-Saxton (GS) algorithm,[4] and Fienup's hybrid input-output method.[5]

The minimum real-space constraint comprises the support of the object, i.e., its spatial dimensions that must be known—at least roughly. In our case the object support is defined by the beam footprint on the sample. Since we measured the beam profile and could fit it with a 2D Gaussian, compare Eq. (1), we defined the support $S(x,y)$ as

$$S(x,y) = \begin{cases} 1 & \text{if } f(x,y) > f(2\sigma_x, 2\sigma_y), \\ 0 & \text{else}, \end{cases} \tag{4}$$

where σ_x is the fitted sigma width projected under 14.76° onto the sample surface, corresponding to 5.43 μm in real space. σ_y is the sigma width perpendicular to the 2Θ direction, corresponding to 1.21 μm. Pixels lying outside that support were assumed to contain no significant real-space amplitudes. Due to the reciprocal-space resolution of $\Delta Q \approx 2.9 \times 10^{-5}$ Å^{-1}, each pixel of the Fourier-transformed 400×400 array corresponded to $\frac{2\pi}{\Delta Q}\frac{1}{400} \approx 54$ nm. The so-defined support, Eq. (4), extended the array in one direction, but still the 2D oversampling ratio was $\sigma=3.47$. In other words, the overall size of the Fourier transform of the diffraction pattern was large enough to fulfill the oversampling condition in 2D, even though the sample area which gave rise to the measured diffraction pattern extended outside the area of the Fourier transform in one direction.

Since the beam profile could be well fitted by a two-dimensional Gaussian, we decided to use a real-space image $\tilde{f}(x,y)$ as possible constraint too, modeled according to

$$\tilde{f}(x,y) = \begin{cases} \alpha f(x,y) & \text{if } f(x,y) > f(2\sigma_x, 2\sigma_y), \\ 0 & \text{else}, \end{cases} \tag{5}$$

where α is an appropriate normalization constant. Figure 4 illustrates the situation.

Thus, the chosen combination of algorithms was GS-HIO. Equation (5) comprised the constraint imposed on the real-space amplitudes during GS cycles (200 per period), i.e.,

$$g_{n+1}(\boldsymbol{x}) = \frac{g_n'(\boldsymbol{x})}{|g_n'(\boldsymbol{x})|}\tilde{f}(\boldsymbol{x}). \tag{6}$$

In the following HIO cycles (600 per period), the real-space step consisted of

$$g_{n+1}(\boldsymbol{x}) = \begin{cases} g_n'(\boldsymbol{x}), & \boldsymbol{x} \notin \gamma, \\ g_n(\boldsymbol{x}) - \beta_{\mathrm{HIO}} g_n'(\boldsymbol{x}), & \boldsymbol{x} \in \gamma, \end{cases} \tag{7}$$

with β_{HIO} the HIO algorithm's constant of proportionality,[5] which was set to $\beta_{\mathrm{HIO}}=0.75$, and γ the set of pixels lying outside the support defined in Eq. (4).

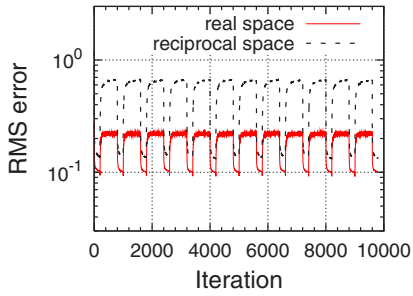

FIG. 5. (Color online) Typical RMS error in real (full red line) and reciprocal space (dashed black line) during 9800 iterations overall. Periodically, 200 GS cycles are followed by 600 HIO steps. The RMS error decreases relatively fast during GS cycles and rises while HIO is applied.

The diffraction peak was centered in the array, in order to minimize artificial phase gradients in the reconstruction result. Overall 100 runs with different sets of random initial phases were done. Each run was stopped after 9800 iterations, since the calculated root-mean-square (RMS) error (in reciprocal and real space) did not fall under a predefined threshold before that cycle limit. The reciprocal-space RMS error after n cycles, $e_{\boldsymbol{Q}}^{(n)}$, was calculated according to

$$e_{\boldsymbol{Q}}^{(n)} = \sqrt{\frac{\sum_{\boldsymbol{Q}} (|G_n(\boldsymbol{Q})| - |F(\boldsymbol{Q})|)^2}{\sum_{\boldsymbol{Q}} |F(\boldsymbol{Q})|^2}}, \tag{8}$$

with $|F(\boldsymbol{Q})|$ the measured diffraction amplitudes and $G_n(\boldsymbol{Q})$ the reciprocal-space estimate after n iterations. In case of the GS cycles the real-space RMS error $e_{\boldsymbol{x}}^{(n)}$ was calculated analogously to Eq. (8), using $\tilde{f}(\boldsymbol{x})$ as real-space amplitudes. In the case of the HIO cycles the real-space RMS error was computed as[28]

$$e_{\boldsymbol{x}}^{(n)} = \sqrt{\frac{\sum_{\boldsymbol{x}\in\gamma} |g_n'(\boldsymbol{x})|^2}{\sum_{\boldsymbol{x}\notin\gamma} |g_n'(\boldsymbol{x})|^2}}, \tag{9}$$

where $g_n'(\boldsymbol{x})$ is the real-space estimate after n iterations. Figure 5 shows typical RMS-error curves for the whole 9800 iterations. The RMS error decreases relatively fast during GS cycles and rises while HIO is applied. From the error curves, no clear convergence can be seen, i.e., a global minimum is not found, and the algorithm stops after the predefined number of overall iterations. However, in order to judge the reconstruction success one must look at the reconstructed real-space phases directly.

Figure 6 shows an example of the reconstructed phase structure $\phi(\boldsymbol{x})$. Clearly, the phase structure within the support region is nonrandom. At first glance, it even resembles a domain structure. However, different runs produce differently looking results. In principle, the correspondence between the reconstructed phase $\phi(\boldsymbol{x})$ and the true phase ϕ_0 is limited by the so-called trivial characteristics.[29] The possible constant offset ϕ_c, for example, which can vary between different reconstruction runs, makes it difficult to draw any clear conclusions by considering $\phi(\boldsymbol{x})$ only. Instead, it is advisable to search for phase jumps, since the latter should be observed at APB's. Note that in principal phase jumps only make sense in the interval $\Delta\phi \in [-\pi, \pi]$. Ideally, the phase jumps due to APB's should be $|\Delta\phi| = \pi$, as was mentioned earlier.

In practice, however, we do not expect to get such sharp phase jumps because our sample is not just a phase-modulating mirror, but has a certain thickness. As was calculated in Eq. (2), the information depth was $t \approx 0.92$ μm. Similarly, estimating the path-length difference (PLD) gives[30] PLD $\approx 2\mu \sin^2 \Theta \approx 0.93$ μm. Having an energy resolution of $\Delta E/E \approx 10^{-4}$, the longitudinal coherence length was[30] $\xi_l \approx \lambda^2/\Delta\lambda \approx 1.47$ μm. Taking the definition of ξ_l seriously, we estimate that scattered photons may get out of phase in our experiment by $(\mathrm{PLD}/\xi_l)\pi \approx 0.63\pi$. From this consideration it would be reasonable to choose an acceptance interval of $|\Delta\phi| \in [0.37\pi, \pi]$ for phase jumps at APB's. In the following, the reconstructed phases from all runs were analyzed with respect to phase jumps $|\Delta\phi| \in [0.35\pi, \pi]$. Figure 7 illustrates the result for the phases shown in Fig. 6.

The most striking feature in Fig. 7 is that there are no closed APB structures present, as one would naively expect in case of a pronounced domain structure. Instead rather straight lines are found. These are, however, preferably oriented parallel to the [110] direction (indicated by the gray arrow in Fig. 7), along which APB's occur in a $B2$ superstructure. One possible explanation for this kind of structure could be grown-in domain walls that start and terminate at dislocations.

Looking at phase-jump patterns from different reconstruction runs, we face the problem that these are not identical with Fig. 7. However, a few characteristic local structures (APB's) are always found, but at different places. To be more precise, there seems to be a lot of noise, not representing any real APB structures, but merely consisting of random structures containing only a few connected (black) pixels. On the other hand, there are a few (three to four) larger characteristic structures that seem to appear in practically all reconstruction runs more or less pronounced, but at different places. Apparently, the reconstruction algorithms fail to reconstruct the long-range structure, but find correct local structures. In order to quantify this finding, i.e., to unambiguously identify unique APB structures in all reconstructed phase-jump patterns, the cross-correlation technique was applied.

In doing so, a mask m, i.e., a small region containing a certain APB structure, was arbitrarily chosen and the normalized cross-correlation coefficients $\gamma(u,v)$ of the mask with the results from the 100 reconstruction runs were determined. The same procedure was done for masks rotated by 180° in order to account for complex conjugated local solutions. The normalized cross-correlation coefficient[31] is defined as

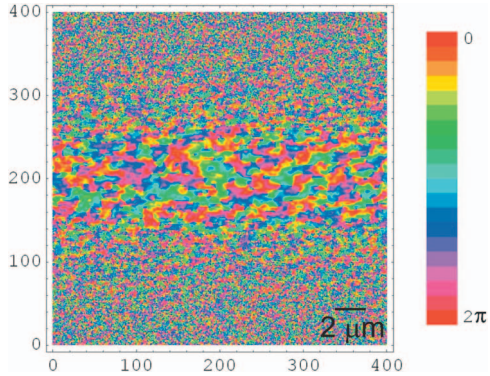

FIG. 6. (Color) Typical reconstructed phases after 9800 iterations with periods of 200 GS and 600 HIO steps. Note the nonrandom phase structure within the support region.

$$\gamma(u,v) = \frac{\sum_{x,y} \{[p(x,y) - \bar{p}_{u,v}][m(x-u,y-v) - \bar{m}]\}}{\sqrt{\sum_{x,y} [p(x,y) - \bar{p}_{u,v}]^2 \sum_{x,y} [m(x-u,y-v) - \bar{m}]^2}}, \tag{10}$$

with $\Sigma_{x,y}$ the sum over x,y under the mask m positioned at (u,v), $\bar{m}$ the mean value of the mask, and $\bar{p}_{u,v}$ the mean of the image pixels p covered by the mask.

Figure 8 shows in the top panel the central rectangular region of Fig. 7 and three masks that were chosen for the cross-correlation analysis. The masks are marked by colored rectangles (blue and green). The middle panel of Fig. 8 shows a phase-jump pattern from another run and the green rectangle indicates where the corresponding mask is found. The position corresponds to the maximum cross-correlation coefficient found in this case ($\gamma_{max}=0.955$), which is illustrated in the bottom panel, where the location of γ_{max} is indicated by a green rectangle. Note that an absolutely perfect cross correlation ($\gamma \equiv 1$) is only rarely obtained. In order to assess the significance of the obtained γ_{max} values, the latter were histogrammed for each mask and its rotated copy. These histograms were fitted with a Gaussian $\propto \exp[-(\gamma_{max} - \gamma_{max}^{(0)})^2/(2\sigma_{\gamma_{max}}^2)]$, as is illustrated in Fig. 9 for the mask which is indicated by the green rectangle in Fig. 8. In this case the fitted mean maximum cross-correlation coefficient was $\gamma_{max}^{(0)}=0.834\pm0.006$ with a standard deviation of $\sigma_{\gamma_{max}}=0.066\pm0.006$. For comparison each mask was cross correlated with artificially generated images, containing random white and black pixels. The resulting γ_{max} values were analyzed in the same way as above, yielding for the same mask as used in Fig. 9 $\gamma_{max}^{(0)}=0.421\pm0.002$ and $\sigma_{\gamma_{max}}=0.039\pm0.002$, for example. This result clearly shows that the obtained γ_{max} values from the cross correlation between the masks and the reconstructed APB patterns are significant and indicate successful findings indeed. Different masks yielded slightly different values, but in all cases the $\gamma_{max}^{(0)}$ values from the cross correlation with reconstructed APB patterns were far beyond any statistics of the random number

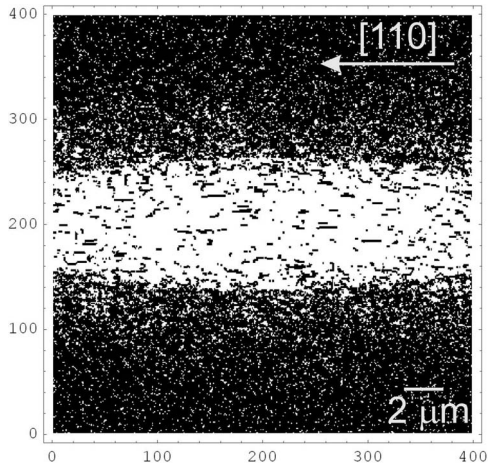

FIG. 7. Visualization of phase jumps in the reconstructed phases of Fig. 6. If the phase difference between a pixel and any of its four nearest neighbors is $|\Delta\phi| \in [0.35\pi, \pi]$, the pixel is shown in black; otherwise white.

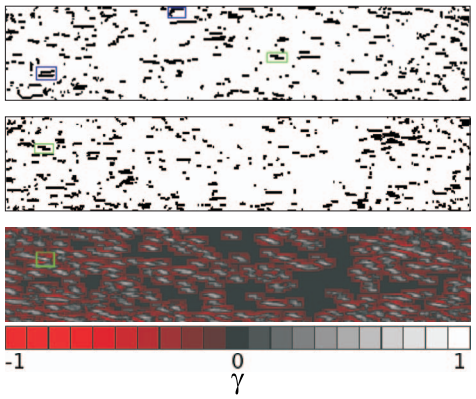

FIG. 8. (Color) Illustration of the cross-correlation analysis. Top: section of phase-jump pattern shown in Fig. 7 with three chosen masks indicated by the blue and green, respectively, rectangles. Middle: phase-jump pattern from another reconstruction run. The green rectangle indicates, where the corresponding mask is found. Bottom: the corresponding cross-correlation coefficient γ with the position of its maximum ($\gamma_{max}=0.955$) surrounded by a green rectangle.

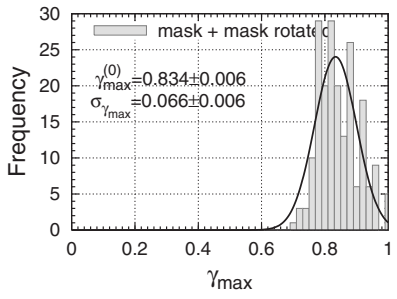

FIG. 9. Histogram of γ_{max} values from cross correlating the mask indicated by the green rectangle in Fig. 8 and its rotated copy, respectively, with results from 100 reconstruction runs. The histogram is fitted with a Gaussian, full black line.

case. More precisely, the $\gamma_{\max}^{(0)}$ values obtained from cross correlations of masks with reconstruction results differed by at least $6\sigma_{\gamma_{\max}}$ from those found in cross correlations with purely random pixel arrays.

We thus conclude that the reconstruction algorithm is successful in finding local structures, but fails in producing a consistent long-range structure, which we attribute to the support, extending the used pixel array in one dimension. Also the fact that we observe an internal quasisymmetry, i.e., a self-similarity of the APB structures, is bad for the phasing algorithms. Furthermore, a lot of noise is present in the reconstructed images, since the number of local structures that are found in all reconstruction runs is rather limited.

Still, what needs to be confirmed is that APB's actually gave rise to the few peculiar, mostly linear structures that can be identified reliably in all reconstruction runs by the cross-correlation technique. On the other hand, one must ask what else could have given rise to such specific phase shifts. Surface roughness can be excluded, since the roughness is something intrinsically irregular and might thus contribute to the noise only, i.e., typically a few connected pixels showing $|\Delta\phi| \in [0.35\pi, \pi]$ in Figs. 7 and 8. For creating the rather long structures (in the order of 1 μm or even longer), which we attribute to APB's, by a certain surface morphology, the surface would have to consist of rather straight steps of corresponding length, similar to the situation in Ref. 27. That scenario can, however, be ruled out considering the polishing of the sample. Another suspicion could be that the shape of the potential APB-phase structures, which is elongated along [110], is just an artifact due to the elongated beam footprint on the sample surface. Looking at the actual numbers of the footprint length and width and comparing them with the lengths and widths of our APB candidates shows that the aspect ratios of the latter are bigger by more than a factor of 2. Thus, the elongated beam footprint cannot explain the observed structures. One alternative explanation for the found structures, which cannot be excluded completely at that point, is that we might see the signature of dislocations instead of APB's. In order to clarify whether indeed APB's are present and what role dislocations play, the sample was further analyzed by means of transmission electron microscopy (TEM).

V. COMPARISON WITH TEM RESULTS

For the TEM analysis, small discs were cut from the same sample and prepared to get thin TEM foils by electropolishing. For observing the APB's, dark-field images using a (010) superlattice reflection were taken with a Philips CM200 operating at 200 kV. Figure 10, top shows a characteristic TEM micrograph with several grown-in APB's. APB's that are inclined to the surface of the TEM foil are *unambiguously* identified by their characteristic fringe contrast. This is clearly demonstrated in the bottom micrograph of Fig. 10, showing a magnified image of the upper right corner. The fringes lying parallel to the surface of the foil are caused by the beam phase shift π occurring at the APB.[32] The periodicity of the fringes with the depth in the foil corresponds to the effective extinction distance ξ_g of the electron beam used to form the image. In the present case $\xi_g \approx 22$ nm, since the dark-field imaging condition, using the weakly reflected beam (010) with (020) in reflecting position, yields a deviation parameter of ≈ 0.04 nm^{-1}. The local change of the fringe spacing and the slight curvature of the fringes along an APB indicate a local variation of the inclination angle. As in the reconstructed images the APB's do not form closed structures. Instead, they comprise preferentially smooth planes near {110} and are bound by superpartial dislocations showing oscillating contrast (cf. D_1 and D_2 in Fig. 10, bottom). The Burgers vector of the bounding superpartial dislocations corresponds to the displacement vector $\langle \frac{1}{2}\frac{1}{2}\frac{1}{2} \rangle$ of the APB, which was deduced by taking images of the same area with different reflection vectors. In addition to the morphology of the APB's, also their sizes found in the reconstruction compare well with those of the TEM results. From these findings it is clear that dislocations cannot explain the characteristic phase-jump patterns found in the reconstruction from the coherent x-ray diffraction of our sample.

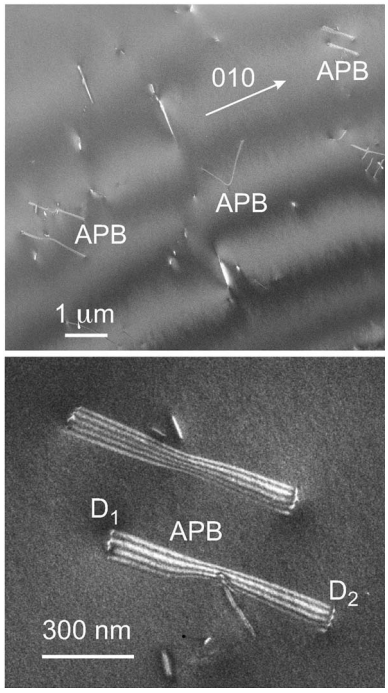

FIG. 10. Top: TEM dark-field image of the $Fe_{65}Al_{35}$ sample, using a weakly reflected beam of the superlattice (010) with a deviation parameter of about 0.04 nm^{-1}. The direction of the imaging vector is indicated by the arrow (direction of incident beam $\approx$[001]). Antiphase-domain walls occur preferentially on {110} planes. Note that the slowly periodic intensity modulation of the image is caused by the increase of the sample thickness from zero (bottom right-hand side) to $\approx$110 nm (top left-hand side). Bottom: zoom of the upper right-hand corner, resolving the characteristic fringe contrast of inclined APB's imaged using a superlattice reflection. The APB's are slightly curved and terminate at superpartial dislocations D_1 and D_2 that show oscillating contrast.

Furthermore, a montage consisting of several adjacent TEM images, taken under similar imaging conditions as those of Fig. 10, confirms that the number of APB's is rela-

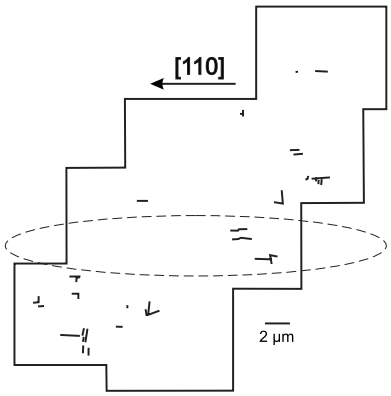

FIG. 11. Map of identified APB's in several adjacent TEM images similar to Fig. 10. The dashed line indicates the area of the support used in the reconstructions for comparison.

tively small. Figure 11 illustrates this finding with a map of identified domain walls. In order to relate the area of this map to the sample area probed in the x-ray experiment, the size of the support used in the reconstructions is indicated by a dashed ellipse. This comparison confirms that only a few true APB's can be expected in the reconstruction results, even though the sample volume probed by the x-ray beam was thicker (information depth $t \approx 0.92\ \mu$m) than in the TEM experiment (average sample thickness ≈ 150 nm).

VI. CONCLUSION

We presented coherent x-ray diffraction imaging results for APB's in a bulk $Fe_{65}Al_{35}$ sample, exhibiting the $B2$ superstructure. Because our sample was much bigger than the beam footprint, knowing the beam profile was key, since the beam defined the region to be reconstructed. This problem was solved by measurements using a CCD camera coupled to an optical microscope. Since antiphase domains are pure phase objects, APB's are mirrored in the reconstructed phases only. Indeed we find phase jumps that we attribute to grown-in APB's. These results are, however, not unique in the sense that a global minimum and a consistent long-range structure, respectively, is not found. Most probably, this is due to the extended support in one direction, which is caused by the projection of the beam onto the sample in reflection geometry and the limited Q resolution. On the other hand, a few characteristic local structures are reconstructed in each run, which is quantified by a cross-correlation analysis. TEM results obtained from the same sample confirm the above findings, since grown-in APB's that strongly resemble the reconstruction results are clearly identified. The APB's, lying preferentially near {110} planes, are only slightly curved and terminate at grown-in dislocations. In the present case the APB structures do not show closed loops and are therefore different from those formed in quenched $B2$-ordered Fe_3Al.[33] It is proposed that the present morphology of APB's is characteristic for annealed alloys having the $B2$-ordered structure up to very high temperatures.

For future investigations of antiphase domains by coherent x-ray diffraction imaging, it seems to be mandatory to overcome the problem of the extended support, i.e., it must be ensured that the support fits into the Fourier-transform array completely. In order to achieve that one could make the incident beam even narrower, further increase the distance between the sample and the detector, or use a detector with smaller pixels.

Another approach would be to apply the so-called Ptychography technique,[17,18] which we anticipate to be the method of choice for overcoming the compactness problem. In applying that method, a series of diffraction patterns is taken, each related to a different, but overlapping region of the specimen. In practice, the sample is moved laterally across the illuminating beam profile, which is selected by a fixed aperture.[18] The overlapping regions allow the degeneracy of structures to be broken, which would be an additional advantage in the case of our $Fe_{65}Al_{35}$ sample, since the self-similarity of the APB structures is bad for the phasing algorithms. Finally, we note that Ptychography techniques have the potential to be a step towards achieving wavelength-limited resolution in electron microscopy, too.[17,34] However, Ptychography has not worked with electron diffraction data up to now. X rays, on the other hand, are closer to the kinematical limit, where inversion and phasing methods can work.

ACKNOWLEDGMENTS

The authors thank C. Rau for providing the optical microscope for measuring the direct beam. Two of the authors (I.K.R. and R.H.) were supported by EPSRC Grant No. EP/D052939/1 and NSF Grant No. DMR 03-08660. The experimental work was carried out at the Advanced Photon Source (APS) beamline 34-ID-C, which was operated by the Materials Research Laboratory of the University of Illinois under DOE Contract No. DEFG02-91ER45439. APS is itself operated under U.S. DOE Contract No. W-31-109-ENG-38. The work was financially supported by the Austrian Federal Ministry for Education, Science and Culture (Contract No. GZ 45.529/2-VI/B/7a/2002), the Austrian Science Fund (FWF) (Contract No. P17775-N02), and the EU Specific Targeted Research Project DYNASYNC (Contract No. NMP4-CT-2003-001516). Data were evaluated using the Schrödinger II(I) cluster of the Vienna University Computer Center.

*lorenz.stadler@desy.de; Present address: Deutsches Elektronen-Synchrotron (HASYLAB), Notkestr. 85, 22607 Hamburg, Germany.

[1] A. Fluerasu, M. Sutton, and E. M. Dufresne, Phys. Rev. Lett. **94**, 055501 (2005).
[2] K. Ludwig, F. Livet, F. Bley, J.-P. Simon, R. Caudron, D. Le Bolloc'h, and A. Moussaid, Phys. Rev. B **72**, 144201 (2005).
[3] Lorenz-M. Stadler, B. Sepiol, J. W. Kantelhardt, I. Zizak, G. Grübel, and G. Vogl, Phys. Rev. B **69**, 224301 (2004).
[4] R. W. Gerchberg and W. O. Saxton, Optik (Jena) **35**, 237 (1972).
[5] J. R. Fienup, Appl. Opt. **21**, 2758 (1982).
[6] J. Miao, P. Charalambous, J. Kirz, and D. Sayre, Nature (London) **400**, 342 (1999).
[7] H. N. Chapman *et al.*, Nat. Phys. **2**, 839 (2006).
[8] S. Marchesini, H. He, H. N. Chapman, S. P. Hau-Riege, A. Noy, M. R. Howells, U. Weierstall, and J. C. H. Spence, Phys. Rev. B **68**, 140101(R) (2003).
[9] Y. Nishino, J. Miao, and T. Ishikawa, Phys. Rev. B **68**, 220101(R) (2003).
[10] I. K. Robinson, I. A. Vartanyants, G. J. Williams, M. A. Pfeifer, and J. A. Pitney, Phys. Rev. Lett. **87**, 195505 (2001).
[11] J. Miao, T. Ishikawa, B. Johnson, E. H. Anderson, B. Lai, and K. O. Hodgson, Phys. Rev. Lett. **89**, 088303 (2002).
[12] H. N. Chapman *et al.*, J. Opt. Soc. Am. A **23**, 1179 (2006).
[13] G. J. Williams, M. A. Pfeifer, I. A. Vartanyants, and I. K. Robinson, Phys. Rev. Lett. **90**, 175501 (2003).
[14] G. J. Williams, M. A. Pfeifer, I. A. Vartanyants, and I. K. Robinson, Phys. Rev. B **73**, 094112 (2006).
[15] I. K. Robinson and I. A. Vartanyants, Appl. Surf. Sci. **182**, 186 (2001).
[16] M. A. Pfeifer, G. J. Williams, I. A. Vartanyants, R. Harder, and I. K. Robinson, Nature (London) **442**, 63 (2006).
[17] H. M. L. Faulkner and J. M. Rodenburg, Phys. Rev. Lett. **93**, 023903 (2004).
[18] J. M. Rodenburg, A. C. Hurst, A. G. Cullis, B. R. Dobson, F. Pfeiffer, O. Bunk, C. David, K. Jefimovs, and I. Johnson, Phys. Rev. Lett. **98**, 034801 (2007).
[19] J. A. Pitney, I. A. Vartaniants, and I. K. Robinson, Proceedings of the SPIE conference on digital image recovery and synthesis IV, 1999, Vol. 3815, p. 199.
[20] J. A. Pitney, Ph.D. thesis, Graduate College of the University of Illinois at Urbana-Champaign, 2000.
[21] I. Vartanyants, C. Ern, W. Donner, H. Dosch, and W. Caliebe, Appl. Phys. Lett. **77**, 3929 (2000).
[22] *Binary Alloy Phase Diagrams*, edited by T. B. Massalski (American Society for Metals, Metals Park, Ohio, 1986).
[23] J. L. Libbert, J. A. Pitney, and I. K. Robinson, J. Synchrotron Radiat. **4**, 125 (1997).
[24] B. X. Yang, M. Rivers, W. Schildkamp, and P. J. Eng, Rev. Sci. Instrum. **66**, 2278 (1995).
[25] A. Taylor and R. M. Jones, J. Phys. Chem. Solids **6**, 16 (1958).
[26] http://www-cxro.lbl.gov/optical_constants/
[27] I. K. Robinson, R. Pindak, R. M. Fleming, S. B. Dierker, K. Ploog, G. Grübel, D. L. Abernathy, and J. Als-Nielsen, Phys. Rev. B **52**, 9917 (1995).
[28] J. Miao, D. Sayre, and H. N. Chapman, J. Opt. Soc. Am. A **15**, 1662 (1998).
[29] R. H. T. Bates, Optik (Jena) **61**, 247 (1982).
[30] G. Grübel and F. Zontone, J. Alloys Compd. **362**, 3 (2004).
[31] In fact, the term "normalized cross-covariance" would be more precise for $\gamma(u,v)$.
[32] *Transmission Electron Microscopy*, edited by D. B. Williams and C. B. Carter (Plenum, New York, 1996).
[33] M. J. Marcinkowski and N. Brown, J. Appl. Phys. **33**, 537 (1962).
[34] H. M. L. Faulkner and J. M. Rodenburg, Ultramicroscopy **103**, 153 (2005).